Research Article

Journal of Environmental Nanotechnology

# Green Synthesis and RSM Optimization of *Endostemon viscosus*-derived α-$MoO_3$ Nanostructures for Supercapacitor Applications

K. Saravana Moorthy[1], S. Balakrishnan[2], A. Balasubramanian[3], S. Amsaveni[4], Gnanasekaran Sasikumar[5*] and G. Arumugam[6]

[1]Department of Computer Science and Engineering, PPG Institute of Technology, Coimbatore, TN, India
[2]Department of Electronics and Communication Engineering, Sona College of Technology, Salem, TN, India
[3]Department of Chemical Engineering, Saveetha Engineering College, Chennai, TN, India
[4]Department of Electronics and Communication Engineering, Nandha College of Technology, Perundurai, TN, India
[5]Department of Mechanical Engineering, GMRIT Deemed to Be University, Rajam, AP, India
[6]Department of Chemical Engineering, Vel Tech High Tech Dr. Rangarajan Dr. Sakunthala Engineering College, Avadi, TN, India
Received: 13.08.2026 Accepted: 31.08.2026 Published: 30.09.2026
*gnanasekaransasikumar@gmail.com

## ABSTRACT

This study introduces a sustainable plant-mediated strategy for preparing electrochemically active α-$MoO_3$ nanostructures using *Endostemon viscosus* leaf extract and evaluates their potential as supercapacitor electrode materials. The aqueous leaf extract was prepared from 10 g of dried leaves in 100 mL of distilled water at 80 °C for 30 min, followed by its reaction with ammonium heptamolybdate precursor solution and subsequent aging, washing, drying, and calcination. XRD confirmed well-crystallized orthorhombic α-$MoO_3$ with an average crystallite size of approximately 28 nm, while TGA indicated satisfactory thermal stability with 91.4% residual mass. FTIR confirmed characteristic Mo=O and Mo–O–Mo vibrations, and FE-SEM revealed agglomerated flake-/sheet-like nanostructures with interconnected porous regions. EDS showed 66.66 wt.% Mo and 33.34 wt.% O, while BET analysis yielded a specific surface area of approximately 118 $m^2 g^{-1}$ and an average pore diameter of 18 nm. Electrochemical measurements demonstrated a maximum specific capacitance of approximately 458 F $g^{-1}$ at 5 mV $s^{-1}$ from CV and 360 F $g^{-1}$ at 0.5 A $g^{-1}$ from GCD. The electrode retained 94.3% of its initial capacitance after 5000 cycles and exhibited low series and charge-transfer resistances of approximately 1.8 and 7.2 Ω, respectively. Overall, the developed α-$MoO_3$ nanostructures exhibited promising electrochemical performance for supercapacitor applications. Future studies should focus on developing complete two-electrode devices and evaluating energy density, power density, long-term cycling stability, and practical operating performance.

**Keywords:** Green synthesis; Supercapacitors; Thermal stability; Charge transfer; Nanoparticles.

## 1. INTRODUCTION

The growing demand for high-performance supercapacitors has intensified the development of advanced electrode materials capable of providing high electrical conductivity, rapid electrochemical charge transfer, active surface area, prolonged cycling stability, and efficient ion diffusion. In particular, electrode architectures possessing redox activity and structural stability are essential for improving pseudocapacitive charge-storage kinetics and overall electrochemical performance (Ganvir *et al.* 2026). Alongside electrochemical performance, increasing attention has been directed toward sustainable synthesis strategies. Green synthesis provides a cost-effective and environmentally benign route for producing functional nanostructures while reducing the dependence on hazardous chemical reagents (Rout *et al.* 2025). Structural and chemical characterization plays role in understanding properties of synthesized materials. X-ray diffraction (XRD) is widely employed to determine crystalline phases, crystallinity, and structural modifications, whereas FTIR provides information regarding functional groups, chemical bonding, and interfacial (Krishnasamy *et al.* 2026).

Plant-derived extracts have attracted considerable attention as natural sources of phytochemicals that can participate in environmentally sustainable nanoparticle synthesis. Ethanolic leaf extract of *Endostemon* contains phenolics, alkaloids, and tannins and exhibits notable antioxidant, antibacterial, selective cytotoxic, and anti-inflammatory activities (Meena *et al.* 2026b). The suitability of this extract for nanomaterial preparation has also been demonstrated through the synthesis of $TiO_2$ nanoparticles exhibiting anatase crystallinity, spherical morphology, particle sizes of approximately 50–110 nm, and good colloidal stability (Meena *et al.* 2026c).

Among transition-metal oxides investigated for electrochemical energy storage, $MoO_3$ has emerged as an attractive pseudocapacitive material because its redox-active structure can support reversible charge-storage reactions (Vadivel *et al.* 2026). Nevertheless, its electrochemical performance can be restricted by conductivity and charge-transport limitations, motivating the development of composites, heterostructures, conductive hybrids, and surface-modified architectures. For example, a $MoO_3$–MC–$SiO_2$–PANI composite demonstrated prolonged operation over 250,000 charge–discharge cycles and a density of 31 Wh $kg^{-1}$, highlighting the benefits of multicomponent electrode architectures for long-term energy storage (Gottam and Srinivasan, 2021). Similarly, electrodeposited $MoO_3$–PANI exhibited improved ion diffusion and electron transport, achieving a specific capacitance of 683 mF $cm^{-2}$ compared with 203 mF $cm^{-2}$ for pristine $MoO_3$ (Patil *et al.* 2026). The addition of additional redox-active and conductive components has further enhanced the electrochemical characteristics of $MoO_3$-based systems. A Co-doped $MoO_3$/carbon nanosphere electrode showed specific capacitance of 1357.97 F $g^{-1}$, energy density of 169.75 Wh kg(Hemapriya *et al.* 2026). Likewise, hierarchical $WS_2$/α-$MoO_3$ provided 715 F $g^{-1}$ with 85% capacitance retention after 6000 cycles, while the asymmetric device reached an energy density of 37.1 Wh $kg^{-1}$ (Kabir *et al.* 2025). $V_2O_5$-decorated $MoO_3$ microplates further demonstrated that heterointerfaces, mixed-valence states, and oxygen vacancies can promote charge-transfer kinetics, with the optimized electrode reaching 1029.17 F $g^{-1}$ and 42.1 Wh $kg^{-1}$ (Pradhan *et al.* 2026).

Highly porous α-$MoO_3$ nanobenzene with nanosheets directly grown on nickel foam exhibited an exceptionally high SC of 3206 F $g^{-1}$ at 1 A $g^{-1}$, an energy density of 111 Wh $kg^{-1}$, and approximately 99.95% capacitance after 3000 cycles (Raza *et al.* 2024). Carbonaceous and semiconductor hybridization represents another effective approach for overcoming transport limitations of $MoO_3$. An RGO–$MoO_3$–$MoS_2$/polyindole nanocomposite achieved 1189.79 F $g^{-1}$, while its symmetric device delivered an energy density of 67.34 Wh $kg^{-1}$ with 81% capacitance retention after 20,000 cycles (Shoeb *et al.* 2025). Similarly, hydrothermally synthesized g-$C_3N_4$@$MoO_3$/NiO showed SC of 1567 F $g^{-1}$ and an ED of 19.72 Wh $kg^{-1}$, demonstrating the advantages of combining conductive and redox-active components (Alotaibi *et al.* 2025). $MoO_3$ doping of single-layer graphene also produced effective p-type doping and approximately three-fold enhancement in areal capacitance relative to pristine graphene, further confirming the beneficial role of $MoO_3$-based interfacial charge transfer (Verma *et al.* 2025). In addition to compositional modification, synthesis conditions and post-treatment strongly influence $MoO_3$ electrochemical behavior. Orthorhombic $MoO_3$ microstructures produced by controlled oxidation at 500 °C showed initial specific capacitance of 179.2 F $g^{-1}$, which increased to 201.7 F $g^{-1}$ following KOH surface activation because of improved accessible surface area (Ondrejka *et al.* 2025).

Despite these advances, most previous investigations have enhanced $MoO_3$ performance through doping, heterostructure formation, conductive-carbon hybridization, polymer incorporation, surface activation, or conventional hydrothermal and chemical synthesis routes. Comparatively limited attention has been directed toward the plant-mediated synthesis of phase-pure α-$MoO_3$ for supercapacitor electrodes, particularly using *Endostemon viscosus* phytochemicals as natural complexing and stabilizing agents. Moreover, the relationship among bio-assisted synthesis, crystalline structure, accessible mesoporosity, and $Mo^{6+}$/$Mo^{5+}$-mediated pseudocapacitive behaviour remains insufficiently established. Therefore, the present study addresses this gap by developing *E. viscosus*-mediated α-$MoO_3$ nanoparticles and correlating their 28 nm crystallite size, 118 $m^2$ $g^{-1}$ surface area, 18 nm mesopore diameter, and electrochemical characteristics with their suitability for sustainable supercapacitor electrodes.

This study investigates the green preparation of $MoO_3$ nanoparticles using *Endostemon viscosus* leaf extract and examines their potential as active electrode materials for supercapacitors. A distinctive aspect of the proposed approach is the phytochemical-assisted formation of porous $MoO_3$ nanostructures with favourable surface characteristics and improved electrochemical response. Particular attention was given to correlating crystalline features, pore characteristics, and electrochemical charge-storage behaviour. The findings establish a bio-assisted fabrication strategy and demonstrate the potential of plant-mediated $MoO_3$ nanostructures for developing scalable, environmentally sustainable, and efficient energy-storage electrodes.

## 2. MATERIALS AND EXPERIMENTAL METHODOLOGY

### 2.1 Raw Materials

Ammonium heptamolybdate tetrahydrate [$(NH_4)_6Mo_7O_{24}\cdot 4H_2O$] was employed as a molybdenum precursor. Fresh *Endostemon viscosus* leaves were obtained from locally available plants in Tamil Nadu. Double-distilled water was utilized for solution preparation, extraction, washing, and other experimental procedures.

### 2.2 Material Characterization

Crystalline structure and phase composition of prepared $MoO_3$ NPs were investigated by PANalytical X'Pert PRO XRD operated with Cu Kα radiation. Chemical bonding and surface functional groups were

examined using a PerkinElmer Spectrum Two FTIR spectrometer (Shalom *et al.* 2026). Nitrogen adsorption–desorption was performed with a Micromeritics ASAP 2020 surface-area analyzer to analyse BET specific pore characteristics and surface area. Thermal behaviour was assessed using a TA Instruments TGA 550 thermogravimetric analyzer. Surface morphology and particle characteristics were examined by a Gemini Zeiss FESEM coupled with an EDS detector for elemental analysis. Electrochemical characteristics were measured using a CH Instruments CHI660E electrochemical workstation.

## 2.3 Green synthesis of $MoO_3$ NPs by *Endostemon viscosus* Extract

$MoO_3$ nanoparticles were prepared through a plant-assisted synthesis process employing *Endostemon viscosus* leaf extract as a bioactive complexing and stabilizing medium. Collected leaves were repeatedly rinsed with deionized water and subsequently shade-dried. Approximately 10 g of dried leaves were added to 100 mL of distilled water and heated at 80 °C for 30 min. After cooling, suspension was passed through filter paper to recover aqueous extract.

For precursor preparation, an aqueous solution of ammonium heptamolybdate tetrahydrate was prepared at an appropriate molar concentration. Subsequently, 50 mL of prepared plant extract was introduced gradually into 100 mL of precursor solution while magnetically stirring at approximately 60 °C. Stirring was continued for 2 h to facilitate interactions between molybdate species and phytochemical constituents. The resulting suspension was maintained for 12 h to promote precursor formation and stabilization. The solid product was separated by centrifugation and washed using deionized water to eliminate soluble impurities and residual organic constituents.

The recovered material was oven-dried at 70 °C for 12 h. Phenolic compounds, flavonoids, and other oxygen-containing phytochemicals present in the leaf extract can coordinate with molybdenum-containing species by carbonyl and hydroxyl functionalities, thereby influencing particle growth, nucleation, and surface stabilization. Similarly, $MoO_3$ NPs were green-synthesized by plant as an eco-friendly stabilizing and reducing agent (Ferozgandhi *et al.* 2025). The dried precursor was subsequently calcined at 500 °C for 3 h to obtain crystalline α-$MoO_3$ nanoparticles.

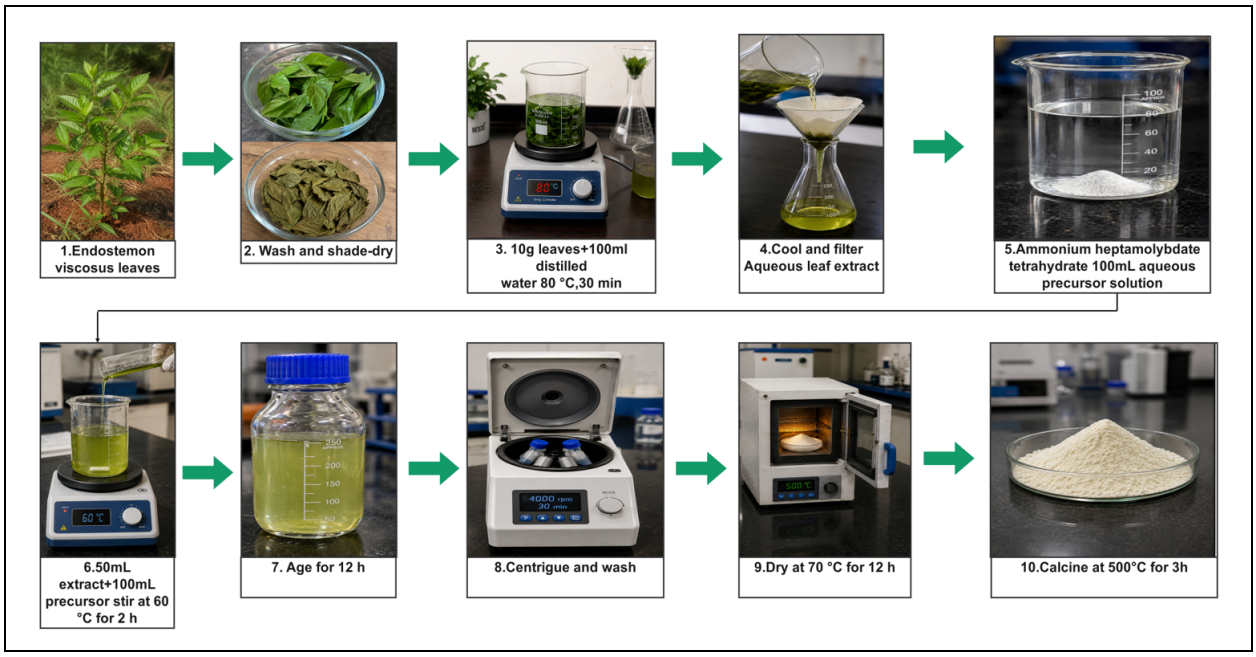


**Fig. 1: Green synthesis of α-$MoO_3$ nanoparticles using *Endostemon viscosus* leaf extract**

## 2.4 Electrochemical Evaluation of $MoO_3$ Electrode

Electrochemical properties were examined by a conventional three-electrode cell with Ag/AgCl as the reference electrode, nickel foam with an exposed area of approximately 1 × 1 cm² as the current collector, and platinum wire as the counter electrode. The working electrode slurry contained 80 wt.% $MoO_3$ active material, 10 wt.% acetylene black, and PVDF. N-methyl was added in sufficient quantity to produce a uniform coating mixture.

PVDF provided mechanical binding and improved adhesion of the electrode layer, whereas acetylene black established conductive pathways for electron transport. Binder and conductive-agent proportions was maintained unchanged for prepared

electrodes. An active-material loading of 4–6 mg $cm^{-2}$ was maintained. Slurry was coated uniformly onto nickel foam and dried at 70 °C for 12 h. Electrode loading was determined from the mass difference of the current collector measured before and after deposition. Identical slurry preparation, coating area, mixing conditions, and drying parameters were maintained to improve experimental reproducibility.

Electrochemical behaviour was investigated by cyclic voltammetry, electrochemical galvanostatic charge–discharge, and impedance spectroscopy (Edlabadkar *et al.* 2026). Impedance measurements were conducted between 0.1 Hz and 100 kHz by sinusoidal perturbation of 10 mV. Gravimetric specific capacitance was determined from the discharge portion of the GCD profile according to:

$$C_s = I\Delta t/(m\Delta V) \quad \ldots (1)$$

where $C_s$ shows specific capacitance (F $g^{-1}$), Δt is the discharge duration, I is the applied discharge current, m corresponds to the mass of $MoO_3$ active material deposited on the electrode, and ΔV shows the effective potential interval during discharge.

## 3. RESULTS AND DISCUSSION

### 3.1 Crystalline Structure, Thermal Behaviour, and Surface Chemistry

XRD was employed to analyse the crystalline phase, structural characteristics, and phase purity of the synthesized material. The diffraction profile was recorded over the 2θ range of 10–80°. Fig. 1 presents the XRD pattern of $MoO_3$ NPs obtained following thermal treatment at 500 °C.

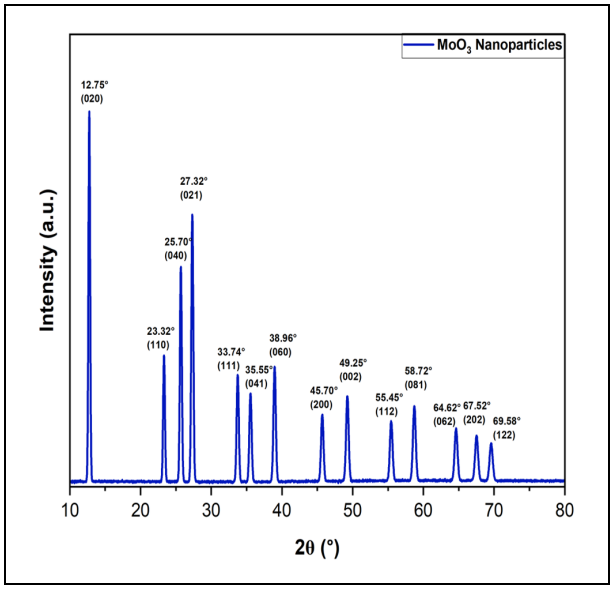


**Fig. 2: XRD profile of green-synthesized $MoO_3$ nanoparticles**

The diffraction reflections are characteristic of orthorhombic α-$MoO_3$, indicating successful development of the crystalline oxide phase. Distinct reflections appeared at approximately 12.75°, 23.32°, 25.70°, 27.32°, 33.74°, 35.55°, 38.96°, 45.70°, 49.25°, 55.45°, 58.72°, 64.62°, 67.52°, and 69.58°, which can be indexed to the (020), (110), (040), (021), (111), (041), (060), (200), (002), (112), (081), (062), (202), and (122) planes, respectively. The absence of prominent secondary-phase reflections indicates good phase purity of the resulting powder. The narrow and intense diffraction peaks further demonstrate appreciable crystallinity. The average crystallite dimension estimated by the Debye–Scherrer relationship was 28 nm. Calculated orthorhombic lattice parameters were approximately a = 3.96 Å, b = 13.86 Å, and c = 3.70 Å, corresponding to a unit-cell volume of about 203 $Å^3$. Recent studies highlighted that the XRD analysis confirmed the successful formation and crystalline phases of Pd–rGO and Pd/$MoO_3$–rGO nanocomposites, including the incorporation of $MoO_3$ nanorods within the Pd–rGO framework. The structural characteristics supported effective interactions among Pd, $MoO_3$, and rGO, contributing to improved electrochemical performance (Wanchan *et al.* 2025).

Thermogravimetric analysis (TGA) and differential thermal analysis (DTA) were performed to evaluate the thermal stability and temperature-dependent transformations of the synthesized $MoO_3$ nanoparticles. The corresponding TG–DTA profiles are shown in Fig. 3.

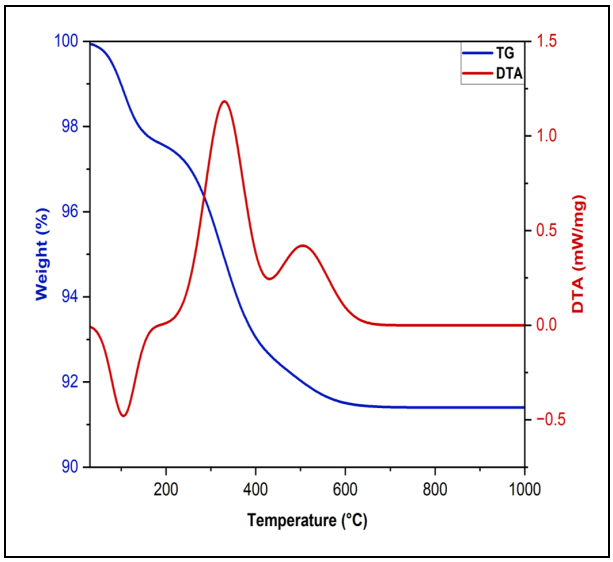


**Fig. 3: TG–DTA profiles of plant-mediated $MoO_3$ nanoparticles**

The TG profile exhibited three principal mass-loss regions. An initial reduction of approximately 2.4% below 150 °C was associated mainly with desorption of physically retained water and surface hydroxyl species, accompanied by a weak endothermic feature near 105 °C.

A second mass reduction of approximately 5.0% between 200 and 400 °C can be attributed to the decomposition of residual organic constituents originating from the bio-assisted synthesis process. A corresponding thermal event appeared near 330 °C. At elevated temperature, an additional mass change of about 1.2% was observed and may be related to the removal of strongly bound residues and high-temperature volatilization processes. Approximately 91.4% of the initial sample mass remained at the end of the measurement, demonstrating satisfactory thermal stability of the synthesized oxide. The mass-loss events below 400 °C align with structural transformations reported for $MoO_3$ nanomaterials; (Zhang *et al.* 2023) identified a first-order h-$MoO_3$-to-α-$MoO_3$ phase transition over 378.5–443.1 °C, driven by release of structurally bound water from octahedral tunnel sites. The thermal event near 330 °C observed here likely reflects an analogous dehydration step preceding transformation to the stable orthorhombic α-$MoO_3$ phase. The high residual mass (91.4%) confirms that the synthesized nanoparticles retain good structural integrity through this transition.

FTIR spectroscopy was employed to identify surface functionalities and characteristic metal–oxygen bonding within the synthesized nanoparticles. The resulting spectrum is presented in Fig. 3.

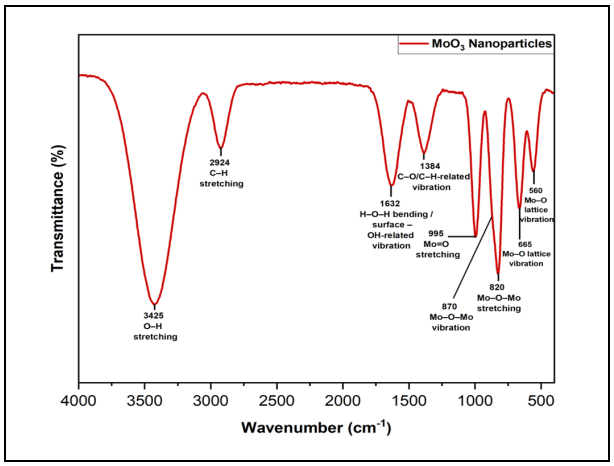


**Fig. 4: FTIR spectrum of bio-assisted $MoO_3$ nanoparticles**

A broad absorption region extending approximately from 3425 $cm^{-1}$ is assigned to O–H stretching from adsorbed water and surface hydroxyl functionalities. The feature around 1632 $cm^{-1}$ is associated predominantly with H–O–H bending of molecularly adsorbed water. Weak bands at approximately 2924 and 1384 $cm^{-1}$ may originate from C–H stretching and residual C–O/C–H-related phytochemical functionalities remaining on the nanoparticle surface. The characteristic terminal Mo=O stretching vibration was observed near 995 $cm^{-1}$, while the bands around 870 and 820 $cm^{-1}$ correspond to Mo–O–Mo vibrations. A lower-frequency feature near 665 and 560 $cm^{-1}$ is associated with Mo–O lattice vibrations. These characteristic absorption features support the development of the Mo–O framework and confirm the formation of $MoO_3$ through the plant-mediated synthesis route. Several reports have indicated that the FTIR analysis confirmed the successful incorporation of $MoO_3$, multilayer graphene (MLG), and coconut husk-derived biochar in the ternary nanocomposite. The observed functional groups supported interactions between $MoO_3$ and the carbonaceous MLG–biochar framework (Saeed *et al.* 2025). Surface features of the synthesized $MoO_3$ NPs were examined through FE-SEM. Fig. 4(a,b) displays the microstructural appearance at two different magnifications.

The micrographs reveal interconnected and agglomerated flake-/sheet-like structures with irregular porous regions. Particle clustering can be associated with surface interactions among adjacent structures during drying and subsequent thermal treatment. Numerous interparticle voids are visible throughout the aggregated morphology, producing accessible pathways that can favour electrolyte penetration and ion migration. Such porous structural networks can increase the electrochemically accessible surface and provide effective contact between neighbouring structures, thereby supporting ion transport and charge-transfer processes during electrochemical operation. Previous studies have revealed that the FE-SEM analysis of nanoparticles green-synthesized by Endostemon viscosus leaf extract revealed predominantly rod-shaped Ag NPs, whereas Chi–Ag NPs exhibited mainly aggregated particles. These morphological differences indicate that chitosan influenced nanoparticle growth and surface organization (Meena *et al.* 2026a).

Elemental composition of the synthesized nanoparticles was further examined through EDS, as presented in Fig. 6.

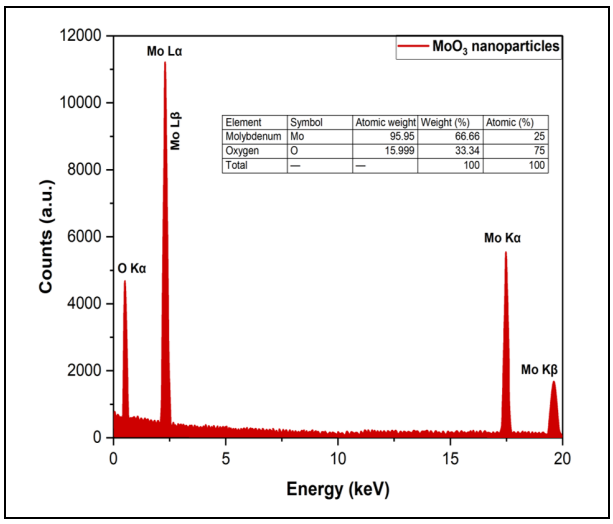


**Fig. 5: EDS spectrum of plant-mediated $MoO_3$ nanoparticles**

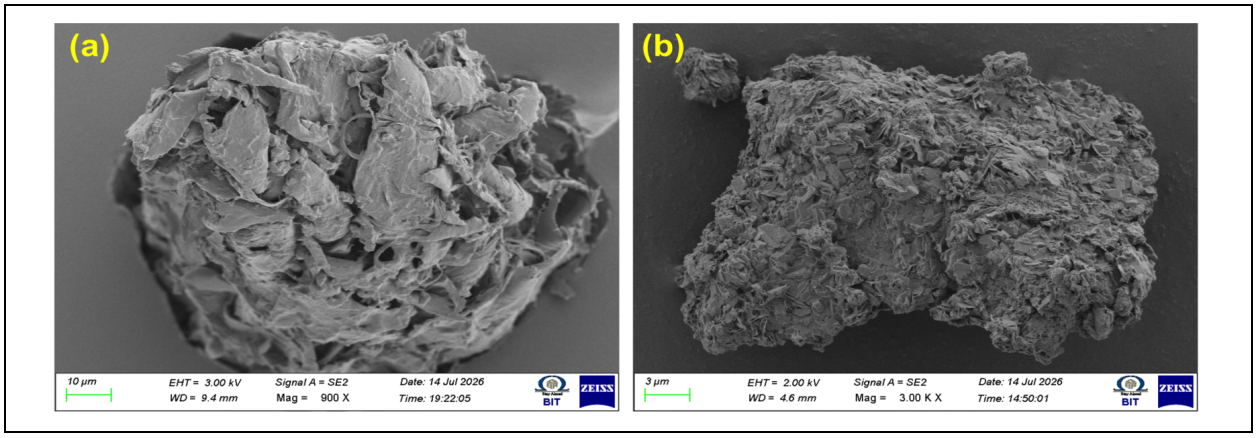


**Fig. 6: FE-SEM micrographs of green-synthesized $MoO_3$ NPs at (a) lower and (b) higher magnification**

The EDS spectrum exhibited prominent signals to Mo and O, confirming these as principal elemental constituents of the prepared material. Quantitative elemental analysis showed approximately 66.66 wt.% Mo and 33.34 wt.% O, corresponding to 25 at % Mo and 75 at. % O, respectively. The atomic ratio of approximately 1:3 (Mo:O) is consistent with the expected $MoO_3$ stoichiometry. No substantial impurity-related signals were observed within the detection capability of the analysis, supporting successful formation of the molybdenum oxide phase. Previous studies have revealed that, the EDS analysis confirmed the presence and successful incorporation of the constituent elements in the $MnO_2$@$MoO_3$/MXene (MMM) composite electrode, supporting the formation of the hybrid structure. The elemental composition indicated effective integration of $MnO_2$ and $MoO_3$ with MXene, contributing to the composite's enhanced electrochemical performance (Eisa *et al.* 2026). Textural characteristics of $MoO_3$ nanoparticles were evaluated from nitrogen adsorption–desorption measurements, as illustrated in Fig. 6(a,b).

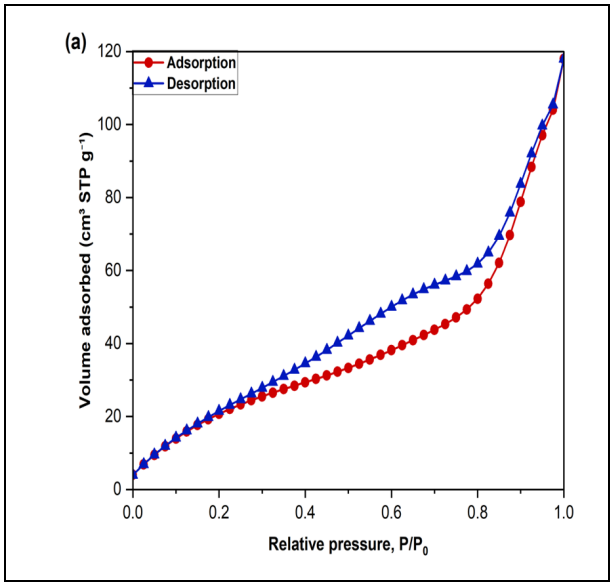


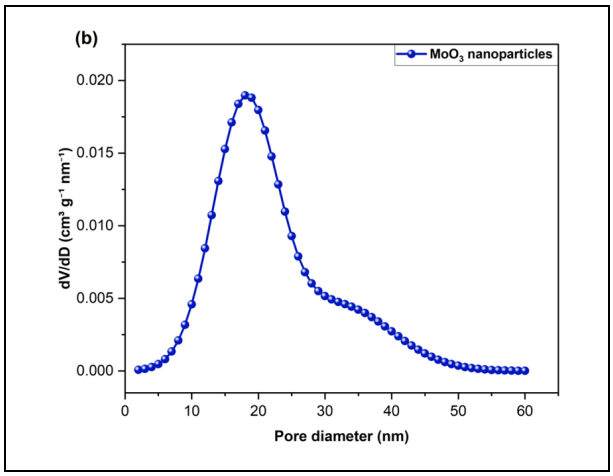


**Fig. 7: (a) Nitrogen adsorption–desorption and (b) pore-size of $MoO_3$ nanoparticles**

BET yielded a specific surface area of approximately 118 $m^2$ $g^{-1}$. The comparatively large accessible surface can be associated with nanoscale particle dimensions, interconnected voids, and porous regions generated between aggregated $MoO_3$ nanostructures. These characteristics provide numerous accessible electroactive sites and shorten electrolyte-ion diffusion pathways. The pore-size distribution has a dominant pore radius of approximately 90 Å, corresponding to an average pore diameter of about 18 nm. This value falls within the mesoporous range and indicates the presence of an interconnected porous architecture. Such mesopores can facilitate electrolyte infiltration, ion transport, and utilization of electrochemical surface sites, thereby contributing to improved charge-storage behaviour. In prior studies, BET analysis confirmed the mesoporous nature of the CuO–$Mo_9O_{26}$ composite, providing an accessible porous structure favorable for electrolyte-ion transport. The mesoporous architecture facilitates ion diffusion and increases accessible electroactive sites, contributing to the enhanced supercapacitor performance (Thirupathy *et al.* 2026).

### 3.2 Electrochemical Performance of $MoO_3$ Electrode

Fig. 7(a) presents cyclic voltammetry responses of the $MoO_3$ electrode obtained at various scan rates.

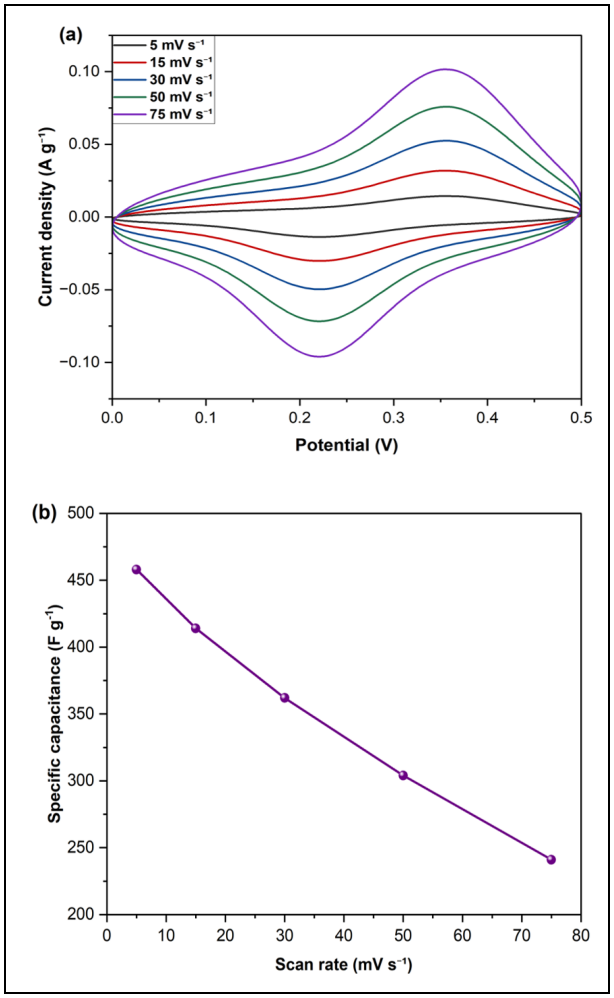


**Fig. 8: (a) CV profiles of the $MoO_3$ electrode and (b) difference of SC with scan rate**

The CV exhibit broad redox features superimposed on a capacitive background, demonstrating that charge storage involves surface capacitive contributions together with Faradaic pseudo-capacitance. The redox response can primarily be associated with reversible changes between $Mo^{6+}$ and $Mo^{5+}$ states accompanied by electrolyte-ion interaction with electrochemically accessible $MoO_3$ sites. Increasing scan rate from 5 to 75 mV $s^{-1}$ produces a corresponding increase in current while largely preserving the overall CV profile, suggesting favourable electrochemical reversibility and relatively rapid charge propagation. Moderate distortion at higher scan rates originates from electrode polarization and restricted ion penetration under rapid potential variation. As reported in previous studies, Cyclic voltammetry (CV) analysis revealed that the electrochemical response of $MoO_3$ nanostructures depended on hydrothermal synthesis temperature and the resulting morphology. The sample synthesized at 220 °C showed the best electrochemical activity, attributed to its higher electrochemically active surface area (ECSA) and greater availability of active sites (Khan *et al.* 2024).

Fig. 7(b) shows the dependence of SC on scan rate. Capacitance progressively decreases as the scan rate increases because only readily accessible surface sites participate effectively at rapid polarization. At slower scanning, electrolyte ions had sufficient time to penetrate the porous electrode architecture and interact at additional redox-active regions. The highest SC of approximately 458 F $g^{-1}$ was at 5 mV $s^{-1}$. As the scan rate increases, the anodic response shifts to more positive potentials, while the cathodic response shifts toward more negative potentials. This increasing separation reflects polarization and kinetic limitations associated with the quasi-reversible $Mo^{6+}/Mo^{5+}$ redox process. The porous nanoscale architecture consequently provides accessible electrochemical sites and shortened pathways for electrolyte-ion migration.

The electrochemical response of $MoO_3$ is closely associated with its multivalent molybdenum chemistry and layered crystal framework. Reversible variation between $Mo^{6+}$ and $Mo^{5+}$ oxidation states contributes to Faradaic charge storage through surface and near-surface reactions. During polarization, charge compensation can occur through reversible insertion and extraction of electrolyte cations within accessible structural regions of $MoO_3$. Structural defects and oxygen-deficient sites can additionally modify electronic transport and provide favourable locations for electrochemical reactions. Furthermore, the mesoporous morphology increases electrode–electrolyte contact and facilitates ion migration toward active sites. The combined contribution of redox reactions, defect charge transport, and accessible porous pathways therefore supports the observed pseudocapacitive response.

Fig. 8(a) displays galvanostatic charge–discharge of $MoO_3$ electrode measured under various applied current densities.

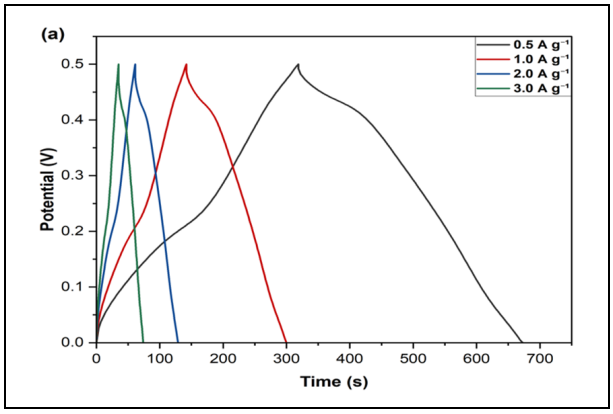

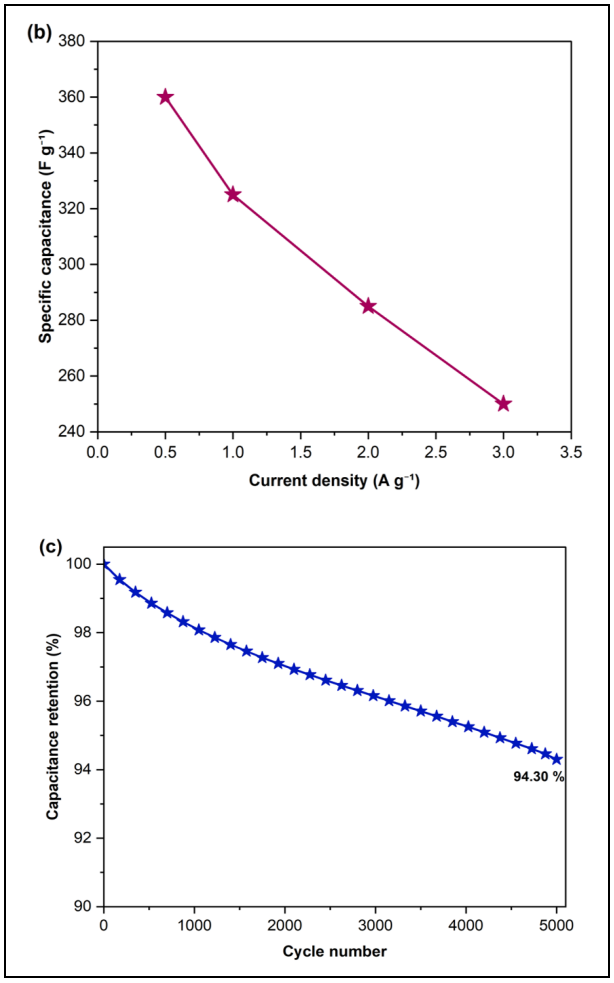


**Fig. 9: (a) GCD profiles of $MoO_3$ electrode at various current densities, (b) specific capacitance and (c) capacitance retention**

The GCD profiles exhibit quasi-symmetric charge and discharge branches with moderate deviation from ideal triangular behaviour, indicating the coexistence of capacitive charge accumulation and Faradaic reactions associated with molybdenum redox centres. The discharge duration progressively shortens with increasing applied current because rapid operation limits electrolyte-ion penetration into less accessible active regions. Nevertheless, the comparable charge and discharge profiles demonstrate favourable reversibility of the electrode reaction.

As illustrated in Fig. 8(b), specific capacitance decreases progressively with increasing current density. At lower current density, electrolyte ions can access a larger fraction of the available surface and near-surface electroactive sites, whereas rapid charge–discharge restricts utilization of deeper regions. Electrode delivered maximum GCD-derived SC of approximately 360 F $g^{-1}$ at 0.5 A $g^{-1}$, decreased to approximately 325, 285, and 250 F $g^{-1}$ at 1.0, 2.0, and 3.0 A $g^{-1}$, respectively. This response can be related to the nanoscale morphology and mesoporous architecture, which improve electrolyte accessibility and provide numerous electrochemically active sites.

The cycling behaviour shown in Fig. 8(c) indicates approximately 94.30% capacitance retention after 5000 cycles, demonstrating satisfactory stability. The gradual reduction during prolonged cycling may arise from minor structural rearrangement, partial loss of accessible active sites, or repeated ion extraction/insertion. Despite this decrease, the electrode maintains substantial electrochemical activity after extended cycling.

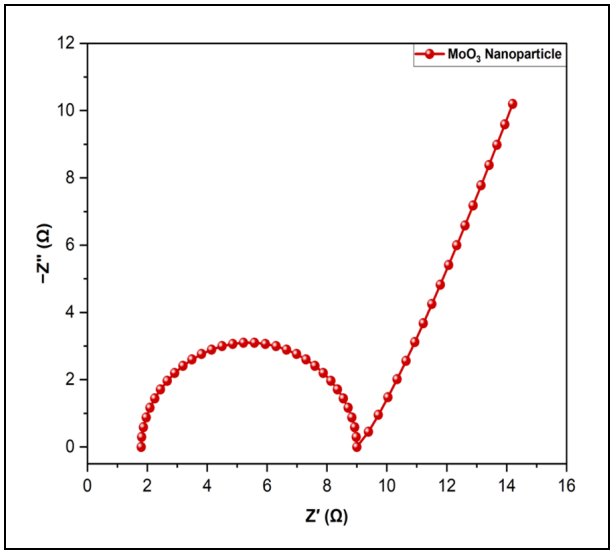


**Fig. 10: Nyquist impedance plot of the $MoO_3$ nanoparticle electrode**

The GCD measurements further demonstrate the favourable charge-storage characteristics of the $MoO_3$ electrode. The nonlinear and quasi-symmetric charge–discharge profiles indicate contributions from both Faradaic and capacitive processes, while the progressive shortening of discharge time with increasing current density reflects the expected rate-dependent behaviour. The electrode exhibited a maximum specific capacitance of approximately 360 F $g^{-1}$ at 0.5 A $g^{-1}$, which gradually decreased with increasing current density, indicating reasonable rate capability. Furthermore, the electrode retained approximately 94.30% of its initial capacitance after 5000 charge–discharge cycles, with good long-term cycling stability. The combination of appreciable specific capacitance, rate capability, and cycling stability can be associated with the accessible nanoscale surface, mesoporous structure, and reversible $Mo^{6+}/Mo^{5+}$ redox activity of the $MoO_3$ electrode. These electrochemical characteristics indicate the potential of the prepared $MoO_3$ nanostructures for energy-storage uses. As reported in previous studies, the GCD analysis showed that the 3% $CdO/MoO_3$ electrode achieved the highest specific capacitance of 671 F $g^{-1}$ at 0.50 A $g^{-1}$, compared with 386 F $g^{-1}$ for pristine $MoO_3$. The enhanced charge–discharge performance was attributed to improved ion-

diffusion electrical conductivity and pathways in the CdO-incorporated $MoO_3$ nanocomposite (Roy *et al.* 2025). Nyquist response obtained at electrochemical impedance spectroscopy is presented in Fig. 9.

The impedance spectrum consists of a high-frequency intercept, a depressed semicircular region, and an inclined low-frequency response. The real-axis intercept represents the equivalent series resistance ($R_s$) with contributions from the current collector, electrolyte, electrode material, and associated contact resistance. An $R_s$ value of approximately 1.8 Ω was obtained, indicating relatively low internal resistance. The high-to-intermediate-frequency semicircle was related primarily to $R_{ct}$. Based on the approximate diameter of the semicircular region, an $R_{ct}$ value of about 7.2 Ω was obtained, indicating comparatively favourable charge-transfer kinetics at the electrode–electrolyte interface.

At lower frequencies, inclined response reflects diffusion-related impedance and capacitive ion accumulation. The porous nanoscale architecture provides pathways for electrolyte penetration and facilitates ion movement toward accessible redox-active regions. Consequently, the combined low series resistance, moderate interfacial resistance, and favourable diffusion response support the capacitive characteristics observed from CV and GCD measurements. Although the three-electrode configuration is appropriate for examining intrinsic electrode behaviour, practical capacitance, energy density, and power characteristics should subsequently be verified using a complete two-electrode supercapacitor device.

## 4. CONCLUSIONS

$MoO_3$ nanoparticles were successfully fabricated through a sustainable plant-assisted route using *Endostemon viscosus* leaf extract. Structural characterization verified the development of a well-crystallized orthorhombic α-$MoO_3$ phase with good phase purity and an average crystallite size of 28 nm. Thermal examination indicated satisfactory stability with limited mass reduction, while FTIR analysis verified characteristic Mo=O, Mo–O–Mo, and Mo–O bonding features. FE-SEM observations revealed agglomerated flake-/sheet-like hierarchical structures with interconnected porous regions. BET evaluation yielded a specific surface area of approximately 118 $m^2\ g^{-1}$ and an average pore diameter of about 18 nm, a mesoporous architecture favourable for electrolyte penetration. Electrochemical measurements demonstrated combined capacitive and Faradaic charge-storage behaviour associated predominantly with reversible $Mo^{6+}/Mo^{5+}$ redox activity. The electrode showed SC of 360 F $g^{-1}$ at 0.5 A $g^{-1}$ and about 94.3% of its capacitance after 5000 cycles. Furthermore, low series resistance of approximately 1.8 Ω and favourable diffusion response indicated effective ion and charge transport. The combined influence of accessible mesoporosity, nanoscale morphology, and multivalent molybdenum redox chemistry demonstrates the potential of bio-assisted $MoO_3$ as an electrode material for sustainable supercapacitors. The proposed synthesis route provides a comparatively simple and environmentally considerate strategy for developing functional metal-oxide materials for electrochemical energy storage.

## FUNDING

This research received no specific grant from any funding agency in the public, commercial, or not-for-profit sectors.

## CONFLICTS OF INTEREST

The authors declare that there is no conflict of interest.

## COPYRIGHT

This article is an open-access article distributed under the terms and conditions of the Creative Commons Attribution (CC BY) license (http://creativecommons.org/licenses/by/4.0/).

## REFERENCES

Alotaibi, N. H., Manzoor, I., Abid, A. G., Shah, J. H., Mohammad, S., Kumar, O. P., Zadneprovskaya, E. V. and Allakhverdiev, S. I., $MoO_3$/NiO bimetallic-N active sites in graphitic nitride sheet for enhanced water splitting and energy storage system, *Int. J. Hydrogen Energy*, 137, 1–12 (2025). https://doi.org/10.1016/j.ijhydene.2025.05.059

Edlabadkar, A. P., Chaudhari, S., Harak, S. S., Vijayakumar, M., Nanthakumar, S. and Mayakannan, S., Optimising Tensile and Impact Strength of Polyethylene-based Nanocomposites with Graphene, Carbon and Hemp Fibers, *Int. J. Veh. Struct. Syst.*, 18(1), 39–46 (2026). https://doi.org/10.4273/ijvss.18.1.08

Eisa, M. H., Esaenwi, S., Okereke, B. O. and Obodo, R. M., Electrochemical engineering on redox-active $MnO_2$ and $MoO_3$ bonded in MXenes matrices for supercapacitor applications, *Inorg. Chem. Commun.*, 185, 116082 (2026). https://doi.org/10.1016/j.inoche.2025.116082

Ferozgandhi, K., Girirajan, M., Subramaniyan, S., Sangaraju, S., Ali, M., Raju, R., Shanmugaraj, G. and Sakkarapani, S., Graphitic carbon nitride quantum dot embedded with $MoO_3$-GO nanosheets as electrode material for enhanced supercapacitor performance, *J. Energy Storage*, 113, 115743 (2025). https://doi.org/10.1016/j.est.2025.115743

Ganvir, H. V, Hadidi, H. M., Saminathan, R., Bhagat, M. S., Krishnaraj, C. and Satishkumar, P., Green Sol–gel Synthesis of Cu/$Co_3O_4$ Nanocomposite Using *Curcuma Longa* Leaf Extract for High-performance Supercapacitor Electrodes, *J. Environ. Nanotechnol.*, 15(1), 543–554 (2026). https://doi.org/10.13074/jent.2026.03.2541993

Gottam, R. and Srinivasan, P., Composite electrode material of $MoO_3$-MC-$SiO_2$-PANI: Aqueous supercapacitor cell with high energy density, 1 V and 250,000 CD cycles, *Polym. Adv. Technol.*, 32(6), 2465–2475 (2021). https://doi.org/10.1002/pat.5276

Hemapriya, S., Velusamy, P., Sivaprakash, P. and Kim, I., Electroactive metal ion ($Co_2^+$) doped $MoO_3$/CNS nanocomposite for high efficiency supercapacitor application, *Electrochimica Acta*, 573, 149450 (2026). https://doi.org/10.1016/j.electacta.2026.149450

Kabir, M. F., Zubair, M. A., Ul-Hamid, A. and Islam, M. R., Enhancing redox activity and surface reactivity via hierarchical α-$MoO_3$ nanobelt incorporation into layered $WS_2$ nanosheets for high performance symmetric and asymmetric supercapacitors, *Nanoscale*, 17(44), 25555–25571 (2025). https://doi.org/10.1039/d5nr03799a

Khan, M., Salman, M., Ullah, A., Ullah, N., Syed, A., Bahkali, A. H., Shah, A., Ali, R., Ling, Y. and Khan, M., Effect of hydrothermal reaction temperature on $MoO_3$ nanostructure properties for enhanced electrochemical performance as an electrode material in supercapacitors, *Ceram. Int.*, 50(19), 34943–34955 (2024). https://doi.org/10.1016/j.ceramint.2024.06.303

Krishnasamy, B., Gladston, A. K., Sekar, C. B. and Selvaraju, M., Investigation on the thermal, mechanical, and morphological characterization of peepal fiber-reinforced epoxy composites enhanced with micro-particulate ziziphus mauritiana seed powder, *Revista Materia*, 31, e20250643 (2026). https://doi.org/10.1590/1517-7076-RMAT-2025-0643

Meena, R., Bharathi, A., Gatasheh, M. K., Ahmed, N. A., Ravindran, B. and Murugesan, S., Green Synthesis of Silver and Chitosan–Silver Nanoparticles Using *Endostemon viscosus* Leaf Extract: Characterization and Biological Activities, *J. Clust. Sci.*, 37(3), 67(2026a). https://doi.org/10.1007/s10876-026-03022-1

Meena, R., Bharathi, A., Gatasheh, M. K., Anis, A. N., Natarajan, D., Ravindran, B. and Murugesan, S., In vitro anticancer and pharmaceutical potential of ethanolic leaf extract of *Endostemon viscosus*, *J. Herb. Med.*, 55, 101081 (2026b). https://doi.org/10.1016/j.hermed.2025.101081

Meena, R., Devaraj, R., Gatasheh, M., Ahamed, A., Ravindran, B. and Murugesan, S., Eco-Friendly Synthesis of Titanium Dioxide Nanoparticles from *Endostemon viscosus* Leaf Extract: Characterization and Evaluation of Biological Activities, *Appl. Organomet. Chem.*, 40(3), e70540 (2026c). https://doi.org/10.1002/aoc.70540

Ondrejka, P., Petrík, A., Husár, M., Straňovský, Á., Kemény, M., Sojková, M., Novák, P. and Mikolášek, M., Optimization of $MoO_3$ microstructures through temperature control and KOH activation for improved supercapacitor electrode performance, *Monatshefte Fur Chemie*, 156(5), 577–582 (2025). https://doi.org/10.1007/s00706-025-03318-4

Patil, A. R., Tawade, A. K., Kamble, G. U., Sharma, K. K. K., Kim, J. H. and Dalavi, D. S., Electrochemical insights into $MoO_3$-PANI composites for enhanced energy storage, *Ionics*, 32(5), 5221–5231 (2026). https://doi.org/10.1007/s11581-026-07074-1

Pradhan, D., Shetgaonkar, S. S., Fernandes, R. and Morajkar, P. P., Hierarchical defect engineered $V_2O_5$-x/$MoO_3$-y microplates as efficient electrode material for enhanced supercapacitor performance, *J. Energy Storage*, 176, 123385 (2026). https://doi.org/10.1016/j.est.2026.123385

Raza, A., Ali, M., Ayub, N., Atta, S. and Jawad, M., Chemical vapor deposition-based synthesis of binder-free nanostructure α-$MoO_3$ electrode material for PES devices, *Physica Scripta*, 99(5), 055910(2024). https://doi.org/10.1088/1402-4896/ad3502

Rout, S. K., Samal, P. K., Panigrahy, J., Nanda, P., Praharaj, S. and Rout, D., Enhanced cyclic stability of $MoO_3$@$BiFeO_3$ nanocomposites for long life supercapacitor electrodes, *J. Alloys Compds.*, 1020, 179422 (2025). https://doi.org/10.1016/j.jallcom.2025.179422

Roy, P., Saifullah, Zubair, M. A. and Islam, M. R., Tuning the electrochemical performance of a hierarchical $MoO_3$/CdO binary heterostructure for supercapacitor applications, *Nanoscale Adv.*, 7(18), 5681–5700 (2025). https://doi.org/10.1039/d5na00491h

Saeed, M., Karamat, S., Alahmadi, A. N. M., Aman, M., Sabir, I., Kashif, M., Masud, M. I. and Ullah, F., Electrochemical behavior of biochar, molybdenum trioxide and graphene nanocomposite for supercapacitors, *Res. Eng.*, 28, 108102 (2025). https://doi.org/10.1016/j.rineng.2025.108102

Shalom, N., Haridass, R., Kulurkar, P. and Mayakannan, S., Development of Eco-Friendly Prosopis Juliflora Fiber-Reinforced Epoxy Composites with Mg $(OH)_2$ and $TiO_2$ Nanofillers for Improved Mechanical and Fire-Retardant Properties, *Int. Res. J. Multidiscipl. Technovat.*, 8(4), 288–306 (2026). https://doi.org/10.54392/irjmt26417

Shoeb, M., Mashkoor, F., Khan, J. A., Gondal, M. A., Kim, B. J. and Jeong, C., Three-dimensionally networked RGO-$MoO_3$-$MoS_2$/polyindole nanocomposite on woven carbon fiber for supercapacitor device and their improved charge storage mechanism, *J. Energy Storage*, 134, 118208 (2025). https://doi.org/10.1016/j.est.2025.118208

Thirupathy, M., Suresh, S., Rajesh, P., Maithreyee, V., Rhoda, J. C., Nagaraja, K. S. and Karnan, C., Supercapacitor performance of binary metal oxide copper (II) oxide-β'-molybdenum oxide nanocomposites for energy storage applications, *J. Alloys Compds.*, 1078, 189715 (2026). https://doi.org/10.1016/j.jallcom.2026.189715

Vadivel, M., Hadidi, M. H., Saminathan, R., Bhagat, S. M. and Satishkumar, P., Synergistic $TiO_2$ Nanosheets and Nitrogen-doped Carbon-coated $NiCo_2O_4$ Nanocomposite for High-performance Hybrid Supercapacitors, *J. Environ. Nanotechnol.*, 15(1), 249–261 (2026). https://doi.org/10.13074/jent.2026.03.2541992

Verma, V., Singh, R. S., Gupta, M. and Singh, A. K., Fermi-level tuning in graphene via green synthesized h-$MoO_3$: Enhanced supercapacitor performance of h-$MoO_3$ doped graphene, *J. Alloys Compds.*, 1018, 179225 (2025). https://doi.org/10.1016/j.jallcom.2025.179225

Wanchan, W., Yogesh, G. K., Yeetsorn, R., Maiket, Y. and Koinkar, P., Synthesis and characterization of synergetic Pd/$MoO_3$–rGO hybrid material as efficient electrode for supercapacitor application, *Mater. Chem. Phy.*, 331, 130134 (2025). https://doi.org/10.1016/j.matchemphys.2024.130134

Zhang, Z., Shi, H., Zhuang, B., Luo, M. and Hu, Z., The microstrain-accompanied structural phase transition from h-$MoO_3$ to α-$MoO_3$ investigated by in situ X-ray diffraction, *Beilstein J. Nanotechnol.*, 14, 692–700 (2023). https://doi.org/10.3762/bjnano.14.55